Monthly Notices of the ROYAL ASTRONOMICAL SOCIETY

MNRAS **526,** 3994–4003 (2023) https://doi.org/10.1093/mnras/stad2966
Advance Access publication 2023 September 28

Exploring the reliability of polar field rise rate as a precursor for an early prediction of solar cycle

Akash Biswas,★ Bidya Binay Karak ★ and Pawan Kumar
Department of Physics, Indian Institute of Technology (Banaras Hindu University), Varanasi 221005, India

Accepted 2023 September 25. Received 2023 September 21; in original form 2023 June 13

ABSTRACT

The prediction of the strength of an upcoming solar cycle has been a long-standing challenge in the field of solar physics. The inherent stochastic nature of the underlying solar dynamo makes the strength of the solar cycle vary in a wide range. Till now, the polar precursor methods and the dynamo simulations that use the strength of the polar field at the cycle minimum to predict the strength of the following cycle have gained reasonable consensus by providing convergence in the predictions for Solar Cycles 24 and 25. Recently, it has been shown that just by using the observed correlation of the polar field rise rate with the peak of the polar field at the cycle minimum and the amplitude of the following cycle, a reliable prediction can be made much earlier than the cycle minimum. In this work, we perform surface flux transport (SFT) simulations to explore the robustness of this correlation against the stochastic fluctuations of bipolar magnetic region (BMR) tilt properties including anti-Joy and anti-Hale type anomalous BMRs, and against the variation of meridional flow speed. We find that the observed correlation is a robust feature of the solar cycles and thus it can be utilized for a reliable prediction of the solar cycle much earlier than the cycle minimum – the usual landmark of the solar cycle prediction.

Key words: dynamo – MHD – Sun: activity – Sun: interior – Sun: magnetic fields – sunspots.

1 INTRODUCTION

The magnetic activity of the Sun determines the space weather conditions of the heliosphere making the study of the dynamics of the Sun's magnetic fields an important aspect in the field of modern Astrophysics. Furthermore, the interaction of the Sun's magnetic fields with the magnetosphere of the Earth can cause various phenomena ranging from the occurrence of beautiful auroras in the polar regions to devastating geomagnetic storms causing malfunction of satellites, loss of communication and navigation systems, disruption in aviation near polar routes, and even large-scale power grid failure on the ground (Gopalswamy 2022). With the growing technological advancement and increasing interest in space exploration over the past few decades, the study of the dynamics and impact of solar magnetism on Earth and on near-Earth space weather has gained tremendous momentum with the aim of achieving enough understanding to safeguard the space-based and ground-based assets against any adversity caused by the Sun's magnetic activities.

The strength of the Sun's magnetic field exhibits cyclic variation with a time period of about 11 yr, which is known as the solar cycle. The underlying mechanism for the solar cycle is believed to be dynamo action operating in the convection zone of the Sun (Karak et al. 2014; Charbonneau 2020). However, the solar cycles are not identical to each other, they exhibit a wide range of variations in their duration and strength as generally measured by the number of sunspots that appear on the solar surface (Biswas et al. 2023). This apparent variation in their strength makes it a very difficult but important task to predict the amplitude of an upcoming solar cycle (Petrovay 2020; Karak 2023). Besides being an outstanding problem in Astrophysics, the reliable prediction of solar activity can help in the planning of upcoming space missions and in the study of space weather.

The Sun's magnetic field can be divided into two components, namely the poloidal and the toroidal components. In the context of the Babcock–Leighton-type solar dynamo theory (Babcock 1961; Leighton 1969), the dynamo operates in a cyclic fashion by producing the toroidal field through the shearing of the poloidal field by the differential rotation of the sun and the poloidal field again gets rebuilt from the toroidal field through the production and decay of the tilted bipolar magnetic regions (BMRs).

The part of the solar dynamo where the poloidal field gets built from the toroidal field experiences some non-linearities (which, at least, include non-linear toroidal flux loss through magnetic buoyancy, Biswas, Karak & Cameron 2022; latitude quenching, Jiang 2020; Karak 2020; and tilt quenching, Jha et al. 2020). This part also involves some stochastic fluctuations (Karak & Miesch 2017; Biswas et al. 2023) mainly due to the inherent randomnesses in the properties of the BMRs (presumably caused by the turbulent nature of the convection). Observations show that the BMR tilt angle consists of significant fluctuations around its mean trend as given by Joy's law (Howard 1991; Jha et al. 2020) and very often BMRs are observed to have wrong tilts (negative tilts, anti-Joy) that do not obey Joy's law and BMRs (anti-Hale) that do not follow Hale polarity rule (Stenflo & Kosovichev 2012; McClintock, Norton & Li 2014). As a result of this stochastic nature, the polar field strength varies significantly from one cycle minima to another, causing subsequent variations in the solar cycle strength (Cameron et al. 2013; Jiang, Cameron & Schüssler 2014; Karak & Miesch 2018; Karak, Mandal & Banerjee 2018; Kitchatinov, Mordvinov & Nepomnyashchikh 2018;

★ E-mail: karak.phy@iitbhu.ac.in (BBK); akashbiswas.rs.phy20@iitbhu.ac.in (AB)

Mordvinov et al. 2022). It has been earlier shown that the anomalous or wrongly tilted BMRs (anti-Hale and anti-Joy type) can have a severe impact on the evolution of the polar field (e.g. Nagy et al. 2017) and can pose a great challenge to the predictability of the solar cycles.

There has been a wide variety of approaches (Petrovay 2020) adopted by various groups in the solar physics community for tackling the problem of predicting the amplitude of Solar Cycles 24 and 25. Amongst them, the predictions based on the polar precursor methods (Schatten et al. 1978; Cameron & Schüssler 2007; Hazra & Choudhuri 2019; Petrovay 2020; Kumar et al. 2021), the dynamo model utilizing the polar field (Choudhuri, Chatterjee & Jiang 2007; Bhowmik & Nandy 2018), and the surface flux transport (SFT) model using observations as inputs (Iijima et al. 2017; Jiang et al. 2018; Upton & Hathaway 2018) have gained a reasonable amount of consensus due to their success in predicting the strength of Cycle 24 (Choudhuri et al. 2007; Jiang, Chatterjee & Choudhuri 2007) and the convergence in their predicted strength of Cycle 25 (Petrovay 2020; Bhowmik et al. 2023; Jiang, Zhang & Petrovay 2023). All these prediction methods are similar to some extent due to the fact that they utilize the strength of the Sun's polar magnetic fields during the solar minima as an input to predict the strength of the following cycle.

Although these methods have provided crucial knowledge about the effectiveness of the solar dynamo and the predictability of the solar cycles, a major drawback of them is that it is required to wait till the solar cycle reaches its minimum in order to reliably predict the strength of the next cycle. On the other hand, the solar minima can be defined only after the cycle has gone past the minima phase and the next cycle has started. In this context, it is of great importance for the solar cycle prediction community to come up with an innovative method for the reliable prediction of solar cycle strength much ahead of the solar minima. This can help a lot in better understanding the predictability of the solar dynamo and gain crucial lead time in space weather awareness.

In the past, studies have cautioned about taking the polar field value much earlier than the cycle minimum for cycle prediction (e.g. Svalgaard, Cliver & Kamide 2005). However, Kumar et al. (2021) argued that from the direct correlation between the polar precursors and the strength of the following cycle, a reliable prediction can be made after 4–5 yr of the reversal of the polar field. Later, Kumar, Biswas & Karak (2022) recently showed that, instead of taking the value of polar field strength at a particular time, if the slope of the polar field build-up (i.e. the rise rate) is considered, then a better correlation with the strength of the following cycle amplitude is obtained. They argued that the physics behind this correlation is linked with the Waldmeier effect (Waldmeier 1935) of the solar cycle and they found the prediction made using the Waldmeier effect (strong correlation between the rise rate and amplitude) matches with the prediction using the polar field rise rate. They used observational data from Wilcox Solar Observatory (WSO) to calculate the average rise rate of the polar field after 3 yr of its reversal (which occurs during the maximum of a cycle) and showed that it is highly correlated with the strength of the upcoming cycle. Their prediction for Cycle 25 using this observed relationship converges reasonably well with other predictions made using polar precursors or dynamo models; see table 2 of Kumar et al. (2022). However, the reliability of the observed correlation could not be checked as the sample size available for the study is limited to only three cycles, although the results from the dynamo model were consistent with observed data.

In this study, we analyse the robustness of this correlation of polar field rise rate with its amplitude and amplitude of the next sunspot cycle against the stochastic nature of BMR properties using SFT simulations. We introduce synthetic spatiotemporal profiles of BMRs mimicking the observed range of their properties in the SFT model to simulate the build-up of the polar field and calculate the amount of toroidal flux to be generated by the simulated polar field through differential rotation to get the strength of the following cycle. The main focus of the study is to understand how the variation in the distribution of tilt of the BMRs and the presence of anti-Hale and anti-Joy BMRs in varied amounts in different phases of the solar cycles impact the predictability of the following cycle using the rise rate of the polar field of the previous cycle. In previous years, there have been multiple studies that have shown that the meridional circulation on the solar surface changes from one cycle to another that impacts the evolution and the statistical properties of the cycles (e.g. Karak 2010; Choudhuri & Karak 2012; Upton & Hathaway 2014; Hazra & Choudhuri 2017). Hence, we also incorporate variations in the speed of surface meridional flow to examine its impact on the aforesaid correlation.

2 MODEL AND SYNTHETIC BMR PROFILE

As the build-up of the poloidal field through the Babcock–Leighton mechanism takes place on the solar surface, we utilize the SFT simulations for our study. Here, we briefly outline the description of the model and the spatiotemporal profile of the BMRs used as the inputs of the model.

2.1 The surface flux transport model

The aim of the surface flux transport (SFT) models is to capture the evolution of the radial magnetic fields on the solar surface under the influence of meridional circulation, differential rotation, and horizontal diffusion (Sheeley, DeVore & Boris 1985; Wang & Sheeley 1989; Baumann et al. 2004). It captures the essence of the Babcock–Leighton framework (Babcock 1961; Leighton 1969) for the decay and dispersal of the tilted BMRs and the transport of the remnant diffused radial flux towards the pole due to meridional circulation that ultimately builds up the polar field. The governing equation at the core of the SFT model is the induction equation of magnetohydrodynamics (MHD) that is of the following form:

$$\frac{\partial \vec{B}}{\partial t} = \vec{\nabla} \times (\vec{v} \times \vec{B} - \eta \vec{\nabla} \times \vec{B}). \tag{1}$$

Assuming the magnetic field is radial on the solar surface, the above equation in the spherical geometry can be written as

$$\begin{aligned}\frac{\partial B_r}{\partial t} = &-\Omega(\lambda)\frac{\partial B_r}{\partial \phi} - \frac{1}{R_\odot \cos\lambda}\frac{\partial}{\partial \lambda}\left[v(\lambda) B_r \cos\lambda\right] \\ &+ \eta_H \left[\frac{1}{R_\odot^2 \cos\lambda}\frac{\partial}{\partial \lambda}\left(\cos\lambda \frac{\partial B_r}{\partial \lambda}\right) + \frac{1}{R_\odot^2 \cos^2\lambda}\frac{\partial^2 B_r}{\partial \phi^2}\right] \\ &+ D(\eta_r) + S(\lambda, \phi, t).\end{aligned} \tag{2}$$

Here, B_r is the surface radial field, $R_\odot$ is the solar radius, λ and ϕ represent the latitude and longitude, respectively. The terms $\Omega(\lambda)$ and $v(\lambda)$ are the differential rotation and the meridional circulation on the solar surface that depend only on the latitude. η_H and η_r represent the horizontal and radial diffusivities, respectively. $D(\eta_r)$ captures the decay of the radial field due to radial diffusion, and $S(\lambda, \phi, t)$ represents the source term of the radial field on the solar surface, in this case, it is the emergence of new BMRs.

For this study, we use the SFT model used in various previous studies such as Baumann et al. (2004), Cameron et al. (2010) etc. with similar profiles and values of the different parameters. Hence, we refrain from an elaborate discussion of the model parameters. However, we mention a few parameters of the model relevant to

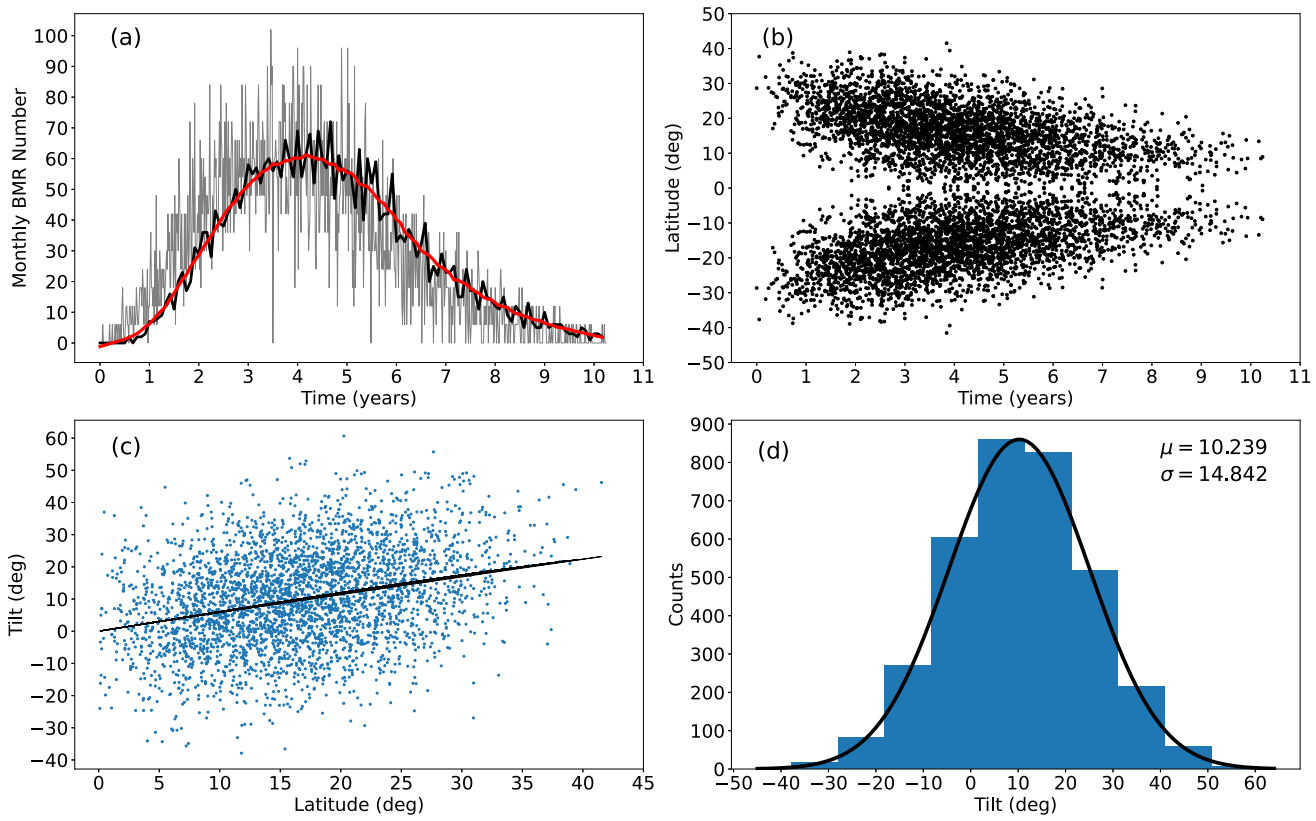

Figure 1. Profile of a synthetic solar cycle (a) and the corresponding butterfly diagram (b). Lower panels represent the properties of the typical tilt distribution used in our study. Panel (c) shows the tilts versus latitudes of BMRs (blue dots), representing the scatter of the BMR tilt around Joy's law (shown as the black solid line), and panel (d) is the distribution of the tilt and the fitted Gaussian profile with standard deviation in the similar range as found in Wang et al. (2015).

this work. The meridional flow on the solar surface, which has been adopted from van Ballegooijen, Cartledge & Priest (1998) and is of the following form:

$$v(\lambda) = \begin{cases} v_0 \sin(2.4\lambda), & \text{where} |\lambda| \leq 75^\circ, \\ 0, & \text{elsewhere}, \end{cases} \tag{3}$$

where we take $v_0 = 22$ m s^{-1} as default in the model. We use the differential rotation profile as prescribed by Snodgrass (1983): $\Omega(\lambda) = \Omega_{\rm eq} - 2.^\circ30 \sin^2\lambda - 1.^\circ62 \sin^4\lambda$ d^{-1}, with $\Omega_{\rm eq} = 13.^\circ38$ d^{-1}.

In the source term $S(\lambda, \phi, t)$, the field of each newly emerged BMR is given by $B_{\rm r} = B_{\rm r}^+ - B_{\rm r}^-$ where

$$B_{\rm r}^{\pm} = B_{\rm max} \left(\frac{0.4 \Delta\beta}{\delta} \right)^2 \exp\left(2[1 - \cos(\beta_{\pm}(\lambda, \phi))/\delta^2] \right), \tag{4}$$

with $\beta_{\pm}(\lambda, \phi)$ as the heliocentric angles between (λ, ϕ) and $(\lambda_{\pm}, \phi_{\pm})$, respectively, $\Delta\beta$ as the separation between the two polarities, and δ as the size or area of the individual patches. The value of $B_{\rm max}$ is taken as 374 G.

2.2 The profile of the synthetic BMRs

We perform the SFT simulations by introducing synthetic BMRs in the model as a source term with properties closely matching with the observations. To generate the synthetic profiles of the spatiotemporal evolution of BMR properties, like the variation of number of BMR emergence with time (profile of the solar cycle) or the profile of the latitudes of the BMR emergence with time (the so-called butterfly diagram) has been adopted from the analytical fittings prescribed by Jiang et al. (2018) and Hathaway, Wilson & Reichmann (1994).

Hathaway et al. (1994) had given a formula for obtaining the smoothed monthly number of BMR emergence in the following form:

$$f(t) = \frac{a(t - t_0)^3}{\exp[(t - t_0)^2/b^2] - c}, \tag{5}$$

where t represents time in months, t_0 is the time of the beginning of the cycle, and a is the cycle amplitude. The parameter b captures the Waldmeier rule of solar cycle (Waldmeier 1935; Karak & Choudhuri 2011), which says stronger cycles rise quickly and is of the form $b(a) = 27.12 + 25.15/(a \times 10^3)^{1/4}$ and $c = 0.71$. More recently this fitting formula has been improved by Jiang et al. (2018) to better fit the latest observational data of Solar Cycles 12–24 using International Sunspot Number Version 2.0. Here we follow the formula prescribed by Jiang et al. (2018) to obtain the monthly number of BMRs. Further, to obtain the daily number of BMR emergence, we divide the cycle in segments of three months and distribute the total number of emerged BMRs randomly over 90 d. This step helps in achieving the observed rapid and stochastic fluctuation in daily BMR numbers; refer to panel (a) of Fig. 1 for the profile of the solar cycle. By comparing Fig. 1 (a-b) with the detected BMRs from magnetograms of the last two solar cycles, as presented in Sreedevi et al. 2023, we note that here we have presented a moderately strong cycle.

Once we have the variation in the number of BMRs with time, we need the information on their latitude and longitudes to deposit

them in the model. The longitudes of the BMRs are randomly chosen for the study. However, the observed range of the latitudinal distribution of the BMRs within a cycle depends on the strength (S_n) of the cycle. For the average latitude of the BMR eruptions, we utilize the same prescription given in section 3.2 of Jiang et al. (2018). Here the mean of the latitude distribution of the BMRs obeys the equation $\lambda_n = (26.4 - 34.2x + 16.1x^2)(\bar{\lambda}_n/14.6)$, where $\bar{\lambda}_n = (12.2 + 0.015S_n)$ and x is the fraction of the solar cycle. The BMRs are randomly distributed around the mean latitude λ_n obeying a Gaussian profile with $\sigma = (0.14 + 1.05x - 0.78x^2)\lambda_n$. In panel (b) of Fig. 1, we present the butterfly diagram obtained by following the mentioned prescriptions and assuming the symmetry in the hemisphere.

Another important parameter of the BMRs is the distribution of their area, which is crucial in determining the total radial flux content of certain BMR. The BMR area (A in μHem) has been randomly drawn from the following lognormal distribution produced from the sunspot group area data as used by previous studies such as Cameron et al. (2010), Jiang et al. (2011) etc.:

$$P(A) = \frac{1}{\sigma_a A\sqrt{2\pi}} \exp\left[-\frac{(\ln A - \mu_a)^2}{2\sigma_a^2}\right], \quad (6)$$

where $\mu_a = 3.79$ and $\sigma_a = 0.68$.

2.3 A note on the distribution of BMR tilt

Here we discuss the most important property of the BMRs for this study, the distribution of their tilt. The tilt of a BMR axis with respect to the equator makes the leading polarity emerge closer to the equator than the trailing polarity, which results into the trailing polarity contributing more to the build-up of the polar fields as it is situated nearer to the pole. Observations show that the BMR tilt (γ) increases with the latitude of emergence following the equation known as Joy's law: $\gamma = \gamma_0 \sin\lambda$ (Hale et al. 1919; Wang & Sheeley 1989; Howard 1991). However, although there is a statistical increase of the tilt with the increase in the latitude of the BMR emergence (similar to Joy's law), there exists a significant scatter in the distribution of the tilt around the value obtained from Joy's law (Howard 1991; Fisher, Fan & Howard 1995; Jha et al. 2020, also see fig. 4 of Karak 2023). This significant scatter in the tilts of the BMRs makes the contributions of the individual BMRs to the build-up of the polar field vary dramatically. Very often it is observed that the tilt is even negative, which makes the leading polarity be situated nearer to the pole and end up contributing oppositely in the build-up of the polar fields, these types of BMRs are known as the anti-Joy type BMRs (e.g. Jiang et al. 2014; Karak & Miesch 2017). In extreme cases, it is seen that the conventional longitudinal orientation (according to the Hale polarity rule; Hale et al. 1919; Stenflo & Kosovichev 2012) of the polarities is flipped. These types of BMRs are known as anti-Hale BMRs that also contribute significantly in the opposite sense to the build-up of the polar fields (Nagy et al. 2017; Mordvinov et al. 2022; Pal et al. 2023).

For the convenience of the understanding regarding the tilts associated with different types of BMRs, we divide them into four major categories as mentioned below:

(i) Hale–Joy regions ($0^\circ < \gamma < 90^\circ$);
(ii) Hale–anti-Joy regions ($-90^\circ < \gamma < 0^\circ$);
(iii) anti-Hale–Joy regions ($-180^\circ < \gamma < -90^\circ$);
(iv) anti-Hale–anti-Joy regions ($90^\circ < \gamma < 180^\circ$).

Here we mention that both the Hale–Joy regions and the anti-Hale–anti-Joy BMRs contribute in a similar manner to the build-up of the polar fields. Hence both these types of BMRs are considered as regular BMRs, however, the latter type of regions are extremely rare in observations. On the other hand, as already discussed, the Hale–anti-Joy (hereafter anti-Joy) and the anti-Hale–Joy (hereafter anti-Hale) type of BMRs are considered as 'anomalous' or 'rogue' BMRs (for pictorial representation of these different types of BMRs, see Muñoz-Jaramillo, Navarrete & Campusano 2021; Pal et al. 2023).

Although it is not clear whether the anti-Hale and anti-Joy type BMRs (so-called 'rogue' or 'anomalous' BMRs) originate through any different mechanisms than the regular BMRs or they are simply the extreme tails of the tilt distribution of the BMRs (Muñoz-Jaramillo et al. 2021), here we incorporate the observed statistical properties to examine their effect on the predictability of the solar cycles. In this work, we take the value of $\gamma_0 = 35^\circ$ following Karak & Miesch (2017) in the equation of Joy's law as mentioned above (we have taken the value of γ_0 slightly higher than the available observations, to avoid the decay of the polar field to extremely lower value in the SFT model.) To capture the scatter in the tilt, we impose a stochastic Gaussian noise around Joy's law, and depending on the value of the μ and σ of the ultimate tilt distribution, a certain percentage of the total BMRs possesses a negative tilt, whereas to obtain the anti-Hale type BMRs, we randomly choose a certain percentage of total BMRs and impose appropriate tilts ($-180^\circ < \gamma < -90^\circ$) to them. The profile of tilt distribution for a certain cycle is shown in the bottom panel of the Fig. 1. We have also investigated the above-mentioned correlation under the impact of tilt scatter dependent on BMR area. Here we mention that the convention of the tilts described here is in the perspective of the Northern hemisphere, the sign of the tilt changes as we consider the Southern hemisphere.

From the information about the coordinates (λ, ϕ) and tilts of the BMRs, the coordinates of the individual poles ($\lambda_\pm$, $\phi_\pm$) are calculated from the following equations:

$$\lambda_\pm = \lambda \pm \frac{\lambda}{|\lambda|}\beta_\pm \sin\gamma \quad \text{and} \quad \phi_\pm = \phi \mp \frac{\lambda}{|\lambda|}\beta_\pm \cos\gamma. \quad (7)$$

2.4 Calculation of polar field and the toroidal field of the following cycle

After introducing the synthetic BMRs in the SFT model, we ran the simulations to study the evolution of the radial photospheric magnetic field. As mentioned above, the deposited BMRs decay due to diffusion and mutual flux cancellation of the opposite polarities. However, a tiny percentage of the remnant diffused radial field from the polarity situated at higher latitude (owing to the tilt of the BMR axis) end up getting advected towards the polar regions by the meridional circulation. To calculate the polar field, we first produce the magnetogram maps of the simulated photospheric fields at every 27 d intervals (the Sun's rotation period at the equator). We take longitudinal averages of these maps that provide us with the latitudinal profile of the radial field. In the next step, we take the average strength of the radial field from 55° to 90° latitudes to obtain the strength of the polar field of each of these maps. This operation is continued for the whole cycle to get the evolution of the polar field throughout the cycle.

For the calculation of the toroidal field to be produced in the following cycle due to the shearing of the polar field by the differential rotation of the Sun, we adopt the prescription provided by Cameron & Schüssler (2015). They showed that by applying Stoke's theorem on the mean-field form of equation (1) in the meridional plane of the Sun along with some simplified and reasonable assumptions, we can

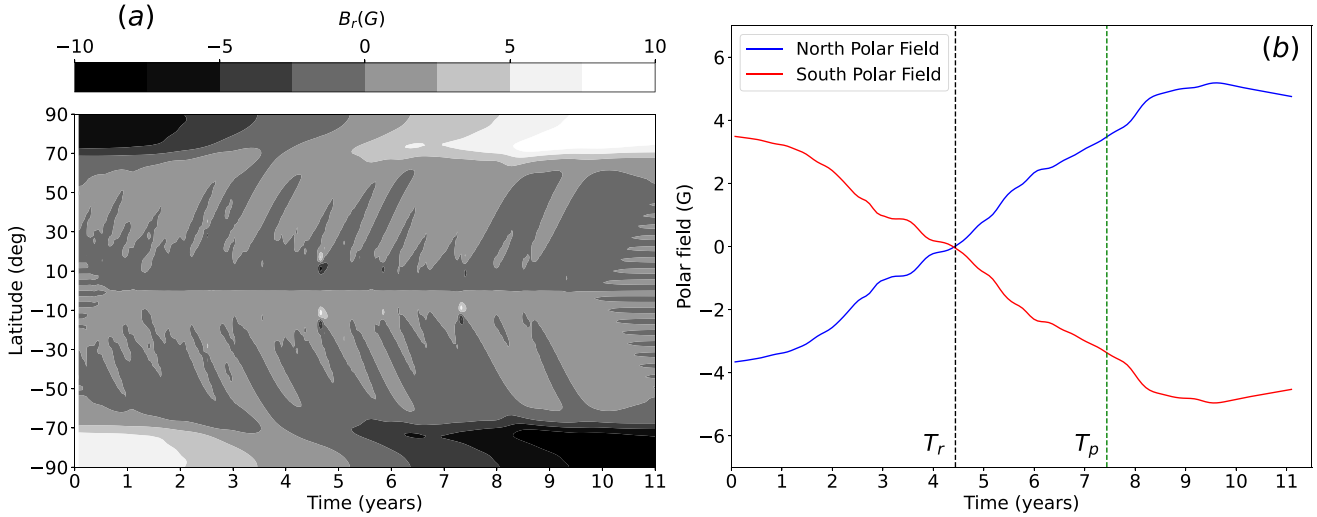

Figure 2. Evolutions of (a) the surface radial field and (b) the polar fields in the SFT simulation throughout the cycle. The black vertical line in panel (b) represents the reversal time (T_r) of the polar fields, and the green vertical line represents the time up to which the polar field data are used to calculate its rise rate, i.e. this is the time (T_p) where prediction can be made about the strength of the peak polar field and about the amplitude of the next cycle.

reach the following equation:

$$\frac{d\Phi^N_{tor}}{dt} = \int_0^1 (\Omega - \Omega_{eq}) B_r R_\odot^2 \, d(\cos\theta) - \frac{\Phi^N_{tor}}{\tau}, \tag{8}$$

where Φ^N_{tor} is the toroidal flux, $\theta (= \frac{\pi}{2} - \lambda)$ is the colatitude, and τ is a parameter representing the diffusion time-scale that is taken to be 4 yr in this work. We solve this equation by taking the surface radial field B_r from the SFT simulations as input to obtain the time evolution of the toroidal flux of the following cycle.

3 METHODOLOGY OF DATA ANALYSIS

In Fig. 2, we present the evolution of the radial surface flux density B_r (panel a) and the evolution of the hemispheric polar fields (panel b) for one of the cycles from our simulation. In the evolution of the polar field, it can be clearly seen that the strength of the polar field is strong during the beginning of the cycle (cycle minimum), and with time it decreases in strength followed by a reversal due to the fields of individual BMR that get transported to the pole by meridional flow as seen in panel (a). This reversal typically happens during the maxima of the cycles. Afterward, the polar field gets built up and reaches its peak during the next minimum due to a further supply of fields from the decaying BMRs. For the prediction of the upcoming cycle strength from the polar precursor methods or by dynamo models, the peak of the polar field at cycle minimum is usually used. However, the determination of the minimum of a solar cycle gets difficult due to the overlap of two consecutive cycles causing rapid fluctuation in sunspot numbers during the last few months of the declining cycle. As a result, to get the value of the polar field peak, one has to wait until the minimum of the cycle has gone past and the polar field has surpassed its peak. In this study, following the previous work of Kumar et al. (2022), we aim to avoid this inconvenience of finding the minima of a cycle and analyse the predictability of the strength of an upcoming cycle much earlier than the minima. We take the time of the polar field reversal (T_r) as the reference time in our calculations, as finding out the reversal of the polar field is comparatively easier and there is no overlap between the two cycles. However, Golubeva et al. (2023) have shown that there is a significant variation in the reversal timings (T_r) of different cycles. It has also been observed that the Sun's polar field reversed multiple times in some cycles (Makarov, Fatianov & Sivaraman 1983; Mordvinov et al. 2022). We also found this kind of multireversal in our simulations due to a large scatter in BMR tilt. In those cases, we take the time of the first reversal as our reference time. From T_r we take the simulated polar field data for the next 3 yr (the green vertical line in panel b indicates the time of prediction, $T_p = T_r + 3$ yr) and calculate the rise rate of the polar field in those 3 yr between T_r and T_p. The polar fields do not rise in a uniform manner throughout those 3 yr but show rapid variations in the initial years. To tackle this issue and to get an average rate of rise of the polar fields, we divide these 3 yr into several overlapping segments and then calculate the rise rate in each of these segments. Finally, the mean rise rate is taken as the ultimate rise rate of the polar fields. In the next step, we find the peak value of the polar field at the end of each cycle and calculate the evolution of the toroidal field to be generated in the next cycle by integrating equation (8). For the amplitude of the next cycle, we take the peak of the calculated toroidal field. Finally, we measure the correlations between the peak strength of the polar field and the peak of the next cycle's toroidal field with the rise rate of the polar field. For different cases of our study, we analyse the impact of fluctuations in the various aforesaid parameters on the correlation between these quantities.

4 RESULTS AND DISCUSSIONS

Before we start discussing the results from the simulations, we would like to mention the features of the solar cycle that can potentially induce the variation in the polar field build-up and subsequently in the polar field rise rate. First, the amplitude of the solar cycles has been observed to vary significantly that leads to variation in the rate of BMR emergence and in turn in the eventual build-up of the polar field. Secondly, the meridional circulation is a key driver behind the transport of the residual field of the disintegrating BMRs toward the poles. Hence, any cycle-to-cycle variation in the amplitude of meridional circulation can impact the growth of the polar field. Lastly, and most importantly, the large scatter in the BMR tilts around

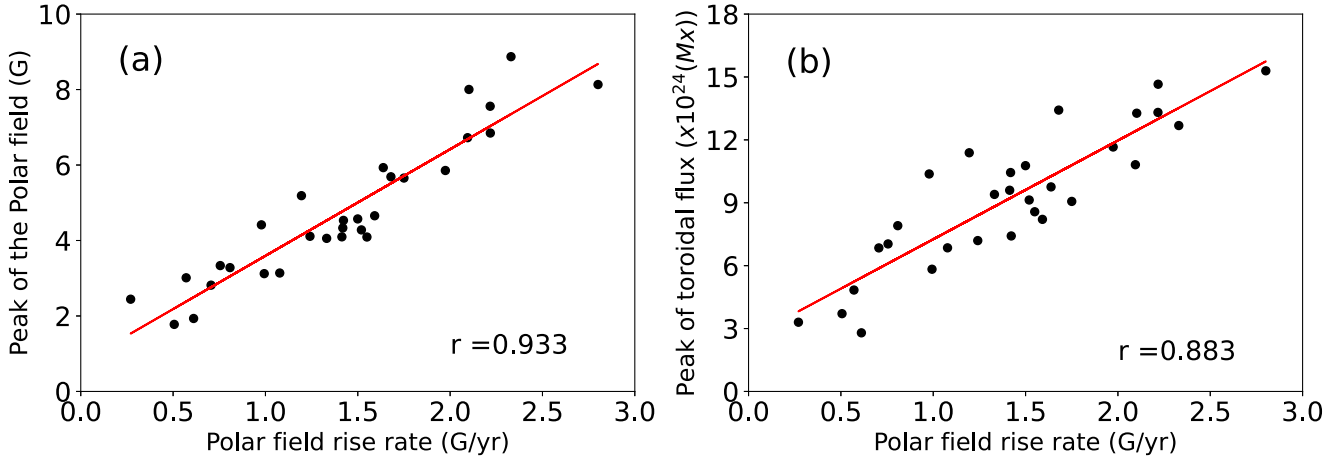

Figure 3. Plot between the rise rate of the polar field and the peak of the polar field (a) and the peak of the next cycle's toroidal field to be produced by the polar field (b). These results are obtained from simulations with variations in cycle amplitudes (Case I).

Joy's law and the variation in the presence of 'anomalous' BMRs can produce significant variation in the aforesaid quantities.

Here, in this section, we will discuss our analysis from the different cases of the simulations using different realizations of the essential parameters of BMR properties and of the model that can impact the polar field build-up as mentioned above. A list of the six major cases of the study is given below.

(I) Variation in cycle amplitudes with BMR tilts strictly following Joy's law.
(II) Same as Case (I), but with varying meridional flow speed in each cycle, i.e. variation in cycle amplitude and in meridional flow speed with BMR tilts strictly following Joy's law.
(III) Variation in the BMR tilt scatter with anti-Hale BMRs presents in all the phases of the cycles.
(IV) Same as Case (III), but with all anti-Hale BMRs in the rising phases of the cycles.
(V) Same as Case (III), but with all anti-Hale BMRs in the declining phases of the cycles.
(VI) Same as Case (III), but with the BMR tilt scatter dependent on the area of the BMRs.

In all of the six cases, the amplitudes of the cycles vary within the range of 30–90 in terms of monthly BMR number. Here we mention that in Case (IV) and Case (V), we include all the 3–7 per cent anti-Hale BMRs within the rising and the decline phases of the cycles. Hence, the temporal density of anti-Hale BMRs is significantly higher in the last two cases than the Case (III) (see Fig. 5) or observations. This is probably not a reality for the actual solar cycles where the anti-Hale BMRs may not show any preference in their presence to the phases of the cycles. However, we create this hypothetical worst-case scenario to test the robustness of the above-mentioned correlation under the impact of a significantly increased temporal density of anti-Hale BMRs in a certain phase of the cycle.

In Fig. 3, we present the results obtained from the simulations for Case (I). In this case, the tilts of the BMRs are obtained from Joy's law (the black straight line in panel c of Fig. 1), i.e. there are no anomalous (anti-Joy or anti-Hale) BMRs in these cycles and the meridional flow speed is the same for all the cycles. However, the amplitudes of the cycles are different from each other that makes the spatiotemporal profile of the BMRs vary from one cycle to the other. This variation in the BMR profile leads to the variation in the build-up of the polar field. It can be seen that the peak of the polar field at the end of each cycle and the strength of the produced toroidal field in the following cycle are very highly correlated with the rise rate of the polar field build-up. A high value of correlation between these quantities infers a better predictability of the strength of a solar cycle from the rise rate of the polar field. In the following four cases, we will include additional stochastic fluctuations in different parameters involved in the model and BMR profiles to examine their impact on this correlation.

Now, we discuss the results from Case (II). The meridional flow speed (v_0) for the cycles is randomly assigned from a uniform distribution in the range $10 \leq v_0 \leq 30$ m s^{-1}. In this case also, the tilts of the BMRs strictly follow Joy's law. The scatter plots obtained from the simulations are presented in Fig. 4. We get a high value of linear Pearson correlation as mentioned in the individual panels of the figure. This result suggests that the variation in meridional circulation does not decrease the correlation between the rise rate and the peaks of the aforesaid quantities, hence it does not have any adverse impact on the predictability of the solar cycles using the rise rate of the polar field.

Before we start the discussion of the rest of the three cases, we present the respective butterfly diagrams presenting the spatiotemporal profiles of the BMRs in each of these cases in Fig. 5. The panels (a), (b), and (c) represent the typical butterfly diagrams of Cases (III), (IV), and (V), respectively. The colour bar in the butterfly diagrams shows the value of BMR tilts, where the blue coloured spots are the anti-Joy BMRs with $-90^\circ < \gamma < 0^\circ$, and the slightly bigger black dots represent the anti-Hale BMRs with $-180^\circ < \gamma < -90^\circ$. In all these three cases, we take the different realization of the tilt properties and the different percentages of anomalous regions in different cycles. Typically, the percentage of the anti-Joy regions varies within a range of roughly 10–30 per cent of the total number of BMRs, on the other hand, we choose the percentage of anti-Hale BMRs within 3–7 per cent, consistent with observations (McClintock et al. 2014). The meridional flow speed is the same for all the cycles in all three cases with $v_0 = 22$ m s^{-1}.

Next, we discuss the results from Case (III) where we randomly deposit the anti-Hale BMRs throughout all the phases of the cycles. The scatter plots for this case are shown in Fig. 6. The value of Pearson correlation coefficients of the polar field rise rate with the peak of the polar field and the peak of the toroidal field is high in this case as well. This result implies that the predictability

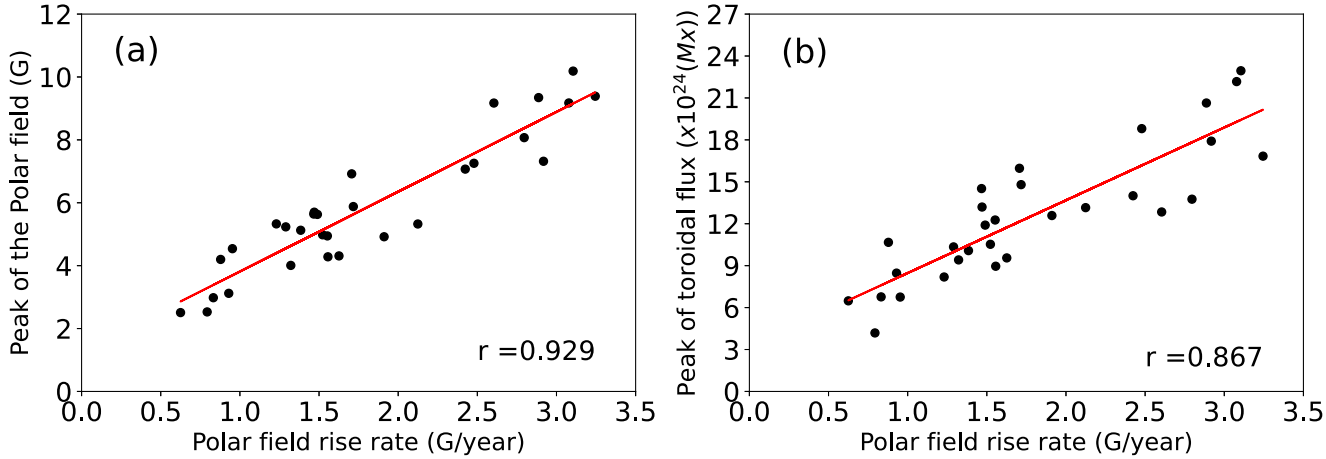

Figure 4. Same as Fig. 3, but for Case (II), i.e. with variation in both the amplitude and in the meridional flow speed of the cycles.

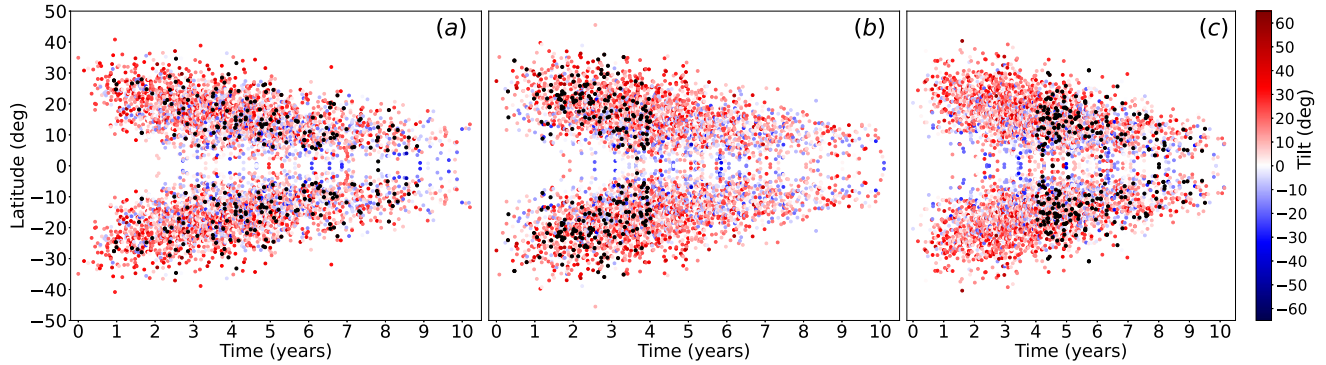

Figure 5. Butterfly diagrams with the different types of BMRs represented by the colour schemes depending on their tilt. The red BMRs are the regular ones with a positive tilt, whereas the blue coloured dots represent the anti-Joy BMRs with a small negative tilt and the bigger black dots are the anti-Hale BMRs. The panels (a), (b), and (c) represent the Cases (III), (IV), and (V), respectively. Note that the colour bar is saturated beyond $\pm 60^{\circ}$ and thus all anti-Hale BMRs appear as black dots.

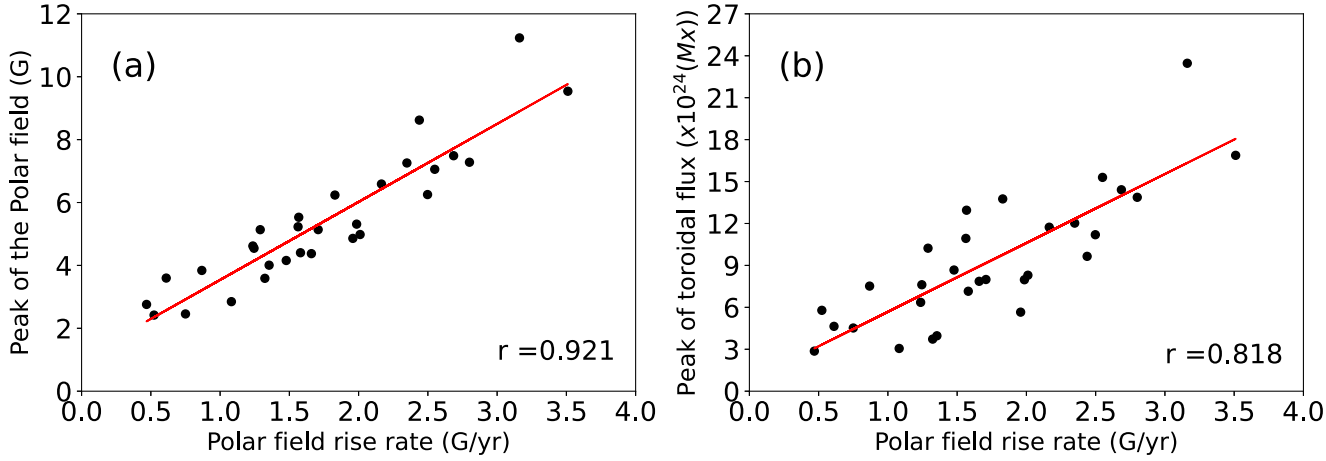

Figure 6. Same as Fig. 3, but for Case (III), i.e. with anti-Hale BMRs deposited throughout all the phases of the cycles.

of the following solar cycle strength does not get affected much even in the presence of significant tilt scatter and the anti-Hale BMRs.

In Fig. 7, we show a similar plot but this time all the anti-Hale BMRs are deposited only in the rising phases of the cycles (Case IV). Again, in this case, the correlation coefficients between the plotted quantities are high and similar in values to the previous two cases. Hence, having a significant amount of anomalous BMRs in the beginning phases of the cycles does not hamper the predictability of the polar field at the cycle minima or the next cycle strength from the polar field rise rate. This is easy to understand because the polar field generated in the rising phase of the cycle is mostly used to reverse

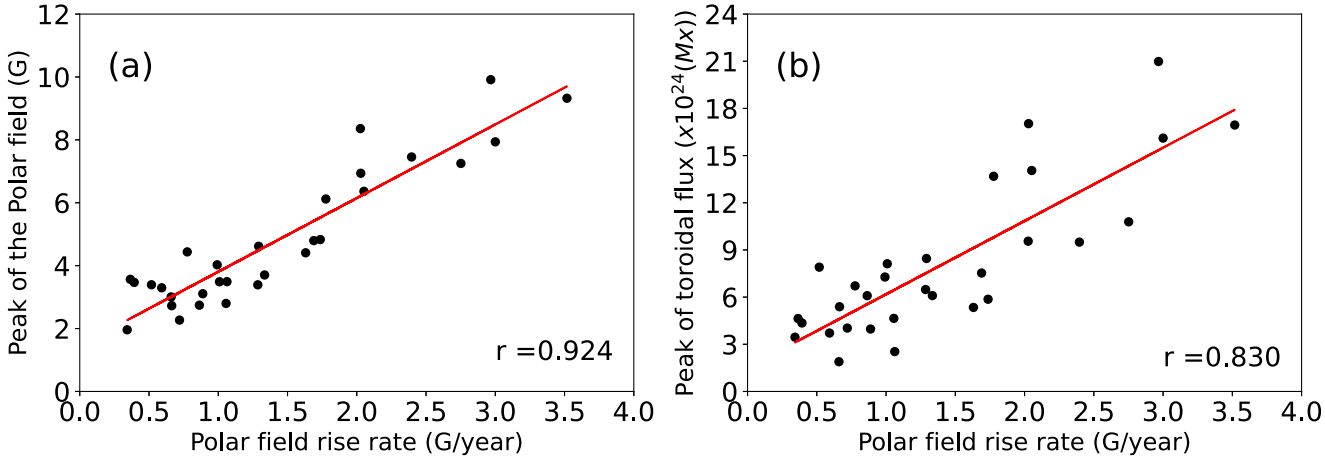

Figure 7. Same as Fig. 3, but for Case (IV), i.e. with anti-Hale BMRs deposited only in the rising phases of the cycles.

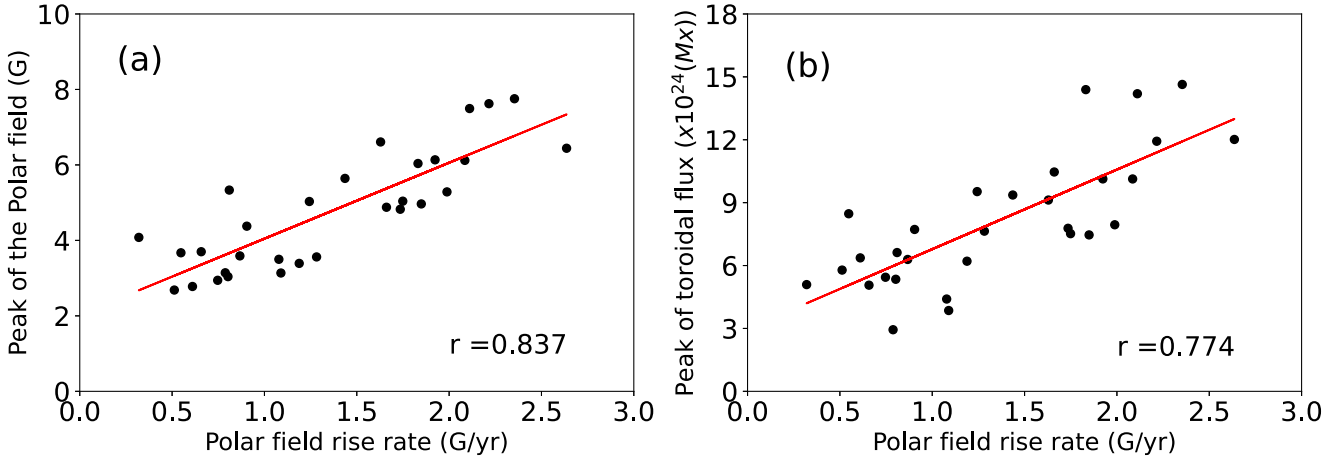

Figure 8. Same as Fig. 3, but for Case (V), i.e. with 'all anti-Hale BMRs' deposited only in the declining phases of the cycles.

the old polarity field and thus the build-up of the polar field after its reversal is undisturbed.

Next, the scatter plots for Case (V) having all the anti-Hale BMRs deposited at the declining phases of the cycles are shown in Fig. 8. In this case, the trends between the plotted quantities are similar to the previous cases, however, a significant drop in the values of the correlation coefficients is observed. This is somewhat expected, as there is a very high concentration of anomalous BMRs during the ending phases of the cycles that significantly diverts the trajectory of the polar field, causing the actual peak to be far from the expected value. The typical evolution of the polar fields for five cycles belonging to Case (V) is presented in Fig. 9. The vertical dashed lines show the reversal time (T_r) and the vertical dashed–dot lines show the prediction time (T_p). In the background, the profile of the solar cycle is shown for reference to the different phases of the cycle along with the typical butterfly diagram. From the evolution of the polar fields, it can be easily inferred that the phase before the reversal exhibits a nearly undisturbed evolution as in this phase the presence of anomalous regions is not significant. On the other hand, just after the reversal, due to the presence of the anti-Hale regions, the growth of the polar field is severely disturbed. As a result, the correlation between the plotted quantities gets worse. However, the values of the correlation coefficients suggest that a decent estimate of the strengths of the polar field and that of the following cycle

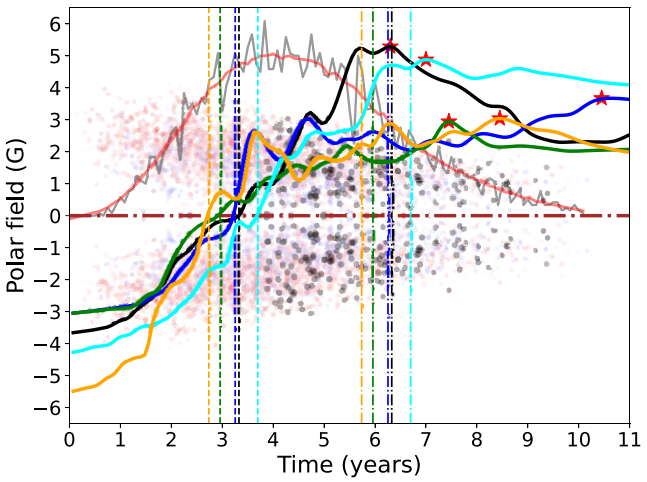

Figure 9. The evolution of northern polar fields for typical five cycles belonging to Case (V). Vertical dashed and dashed–dot lines, respectively, represent the T_r and T_p of the individual cycles. The typical variation of the BMR number (similar to panel a of Fig. 1) is shown in the background for the temporal reference regarding the phase of the solar cycles. The butterfly diagram with the tilt information (similar to panel c of Fig. 5) has also been presented in the background. The red asterisk symbols represent the peaks of the polar fields.

can be obtained from the rise rate even in this case as well, but with reasonably wider error bars.

It has been observed that the tilt scatter or the standard deviation (σ) of the tilt distribution shows a significant and systematic dependence on the area of the BMRs. To check whether this dependence impacts the predictability of the solar cycle, we perform the simulations for Case (VI) where we have reinvestigated Case (III) with the area-dependent σ of the tilt distribution that is obtained from the formula given by Jiang et al. (2014). In this case, from the simulation of 30 cycles, we have obtained strong correlation coefficients of 0.903 and 0.851 between the polar field rise rate and the polar field amplitude and the following cycle amplitude, respectively. This result emphasizes that there is not much impact of the area-dependent tilt scatter on the correlation between these quantities. The p values of all these correlations have not been presented as their values are much smaller ($<10^{-7}$) than the significance level.

5 CONCLUSION

In conclusion, we find that the strong correlation between the polar field rise rate a few years after the cycle maximum with the peak of the polar field (at the cycle minimum) and the strength of the following sunspot cycle, as first shown in Kumar et al. (2022), is a robust feature of the solar cycle. Our extensive simulations using the SFT model suggest that this relation between the aforesaid quantities can be utilized to reliably forecast the strength of the upcoming solar cycle much earlier than the cycle minimum. For our study, we have taken data from only the first 3 yr from the first reversal of the polar field (T_r to T_p) that happens during the cycle maximum. It is to be noted that, even in the cases of multireversals in the polar field, we get the high correlation between the above quantities by taking the first reversal time as T_r. We find that cycle-to-cycle variation of meridional flow speed does not have any impact on the predictability of the solar cycle using this method. We get a very high correlation between the peaks of the following cycle with the rise rate of the polar field even in the presence of anomalous BMRs throughout the cycles consistent with observation. However, a high concentration of anomalous BMRs present during the declining phase of the cycles hampers this correlation to some extent, but still the correlation is strong enough to provide a reasonable forecast of the upcoming cycle's strength.

ACKNOWLEDGEMENTS

The authors are grateful to Dr Robert Cameron for kindly providing the SFT code used in this study and for providing important insights regarding the results during several discussions. The authors also thank Professor Kristof Petrovay for fruitful discussions that benefitted this project. The authors are thankful to the anonymous referee for carefully reviewing the manuscript and for providing insightful suggestions to improve the quality of the paper. AB acknowledges financial support from the University Grants Commission, Government of India. AB and BBK acknowledge the financial support from the ISRO/RESPOND program (project no. ISRO/RES/2/430/19-20) and Ramanujan Fellowship (project no. SB/S2/RJN-017/2018). This study benefitted from financial support provided by the International Space Science Institute (ISSI Team 474).

DATA AVAILABILITY

In this work, we have performed the simulations using the SFT code as mentioned in Baumann et al. (2004). The code for the synthetic BMR profile and the data from the SFT simulations along with the codes for the data analysis can be shared upon a reasonable request.

REFERENCES

Baumann I., Schmitt D., Schüssler M., Solanki S. K., 2004, A&A, 426, 1075
Bhowmik P., Jiang J., Upton L., Lemerle A., Nandy D., 2023, Space Sci. Rev., 219, 40
Bhowmik P., Nandy D., 2018, Nat. Commun., 9, 5209
Biswas A., Karak B. B., Cameron R., 2022, Phys. Rev. Lett., 129, 241102
Biswas A., Karak B. B., Usoskin I., Weisshaar E., 2023, Space Sci. Rev., 219, 19
Cameron R. H., Dasi-Espuig M., Jiang J., Işık E., Schmitt D., Schüssler M., 2013, A&A, 557, A141
Cameron R. H., Jiang J., Schmitt D., Schüssler M., 2010, ApJ, 719, 264
Cameron R., Schüssler M., 2007, ApJ, 659, 801
Cameron R., Schüssler M., 2015, Science, 347, 1333
Charbonneau P., 2020, Living Rev. Sol. Phys., 17, 4
Choudhuri A. R., Chatterjee P., Jiang J., 2007, Phys. Rev. Lett., 98, 131103
Choudhuri A. R., Karak B. B., 2012, Phys. Rev. Lett., 109, 171103
Fisher G. H., Fan Y., Howard R. F., 1995, ApJ, 438, 463
Golubeva E. M., Biswas A., Khlystova A. I., Kumar P., Karak B. B., 2023, MNRAS, 525, 1758
Gopalswamy N., 2022, Atmosphere, 13, 1781
H. Babcock, 1961, ApJ, 133, 572
Hale G. E., Ellerman F., Nicholson S. B., Joy A. H., 1919, ApJ, 49, 153
Hathaway D. H., Wilson R. M., Reichmann E. J., 1994, Sol. Phys., 151, 177
Hazra G., Choudhuri A. R., 2017, MNRAS, 472, 2728
Hazra G., Choudhuri A. R., 2019, ApJ, 880, 113
Howard R. F., 1991, Sol. Phys., 136, 251
Iijima H., Hotta H., Imada S., Kusano K., Shiota D., 2017, A&A, 607, L2
Jha B. K., Karak B. B., Mandal S., Banerjee D., 2020, ApJ, 889, L19
Jiang J., 2020, ApJ, 900, 19
Jiang J., Cameron R. H., Schmitt D., Schüssler M., 2011, A&A, 528, A82
Jiang J., Cameron R. H., Schüssler M., 2014, ApJ, 791, 5
Jiang J., Chatterjee P., Choudhuri A. R., 2007, MNRAS, 381, 1527
Jiang J., Wang J.-X., Jiao Q.-R., Cao J.-B., 2018, ApJ, 863, 159
Jiang J., Zhang Z., Petrovay K., 2023, J. Atmos. Sol. Terr. Phys., 243, 106018
Karak B. B., 2010, ApJ, 724, 1021
Karak B. B., 2020, ApJ, 901, L35
Karak B. B., 2023, Living Rev. Sol. Phys., 20, 3
Karak B. B., Choudhuri A. R., 2011, MNRAS, 410, 1503
Karak B. B., Jiang J., Miesch M. S., Charbonneau P., Choudhuri A. R., 2014, Space Sci. Rev., 186, 561
Karak B. B., Mandal S., Banerjee D., 2018, ApJ, 866, 17
Karak B. B., Miesch M., 2017, ApJ, 847, 69
Karak B. B., Miesch M., 2018, ApJ, 860, L26
Kitchatinov L. L., Mordvinov A. V., Nepomnyashchikh A. A., 2018, A&A, 615, A38
Kumar P., Biswas A., Karak B. B., 2022, MNRAS, 513, L112
Kumar P., Nagy M., Lemerle A., Karak B. B., Petrovay K., 2021, ApJ, 909, 87
Leighton R. B., 1969, ApJ, 156, 1
Makarov V. I., Fatianov M. P., Sivaraman K. R., 1983, Sol. Phys., 85, 215
McClintock B. H., Norton A. A., Li J., 2014, ApJ, 797, 130
Mordvinov A. V., Karak B. B., Banerjee D., Golubeva E. M., Khlystova A. I., Zhukova A. V., Kumar P., 2022, MNRAS, 510, 1331
Muñoz-Jaramillo A., Navarrete B., Campusano L. E., 2021, ApJ, 920, 31
Nagy M., Lemerle A., Labonville F., Petrovay K., Charbonneau P., 2017, Sol. Phys., 292, 167
Pal S., Bhowmik P., Mahajan S. S., Nandy D., 2023, ApJ, 953, 51
Petrovay K., 2020, Living Rev. Sol. Phys., 17, 2
Schatten K. H., Scherrer P. H., Svalgaard L., Wilcox J. M., 1978, Geophys. Res. Lett., 5, 411
Sheeley N. R. J., DeVore C. R., Boris J. P., 1985, Sol. Phys., 98, 219
Snodgrass H. B., 1983, ApJ, 270, 288
Sreedevi A., Jha B. K., Karak B. B., Banerjee D., 2023, ApJS, 268, 58

Stenflo J. O., Kosovichev A. G., 2012, ApJ, 745, 129
Svalgaard L., Cliver E. W., Kamide Y., 2005, Geophys. Res. Lett., 32, L01104
Upton L. A., Hathaway D. H., 2018, Geophys. Res. Lett., 45, 8091
Upton L., Hathaway D. H., 2014, ApJ, 792, 142
van Ballegooijen A. A., Cartledge N. P., Priest E. R., 1998, ApJ, 501, 866
Waldmeier M., 1935, Astron. Mitteilungen Eidgenössischen Sternw. Zurich, 14, 105
Wang Y.-M., Colaninno R. C., Baranyi T., Li J., 2015, ApJ, 798, 50
Wang Y.-M., Sheeley N. R., Jr, 1989, Sol. Phys., 124, 81

This paper has been typeset from a TEX/LATEX file prepared by the author.